MATERIALS SCIENCE

Disproportionation chemistry in K_2PtCl_4 visualized at atomic resolution using scanning transmission electron microscopy

Jacob G. Smith[1,2]†‡, Kaustubh J. Sawant[3]†, Zhenhua Zeng[3]*, Tim B. Eldred[2]§, Jianbo Wu[1,4,5]*, Jeffrey P. Greeley[3], Wenpei Gao[1,2,4]*

The direct observation of a solid-state chemical reaction can reveal otherwise hidden mechanisms that control the reaction kinetics. However, probing the chemical bond breaking and formation at the molecular level remains challenging because of the insufficient spatial-temporal resolution and composition analysis of available characterization methods. Using atomic-resolution differential phase-contrast imaging in scanning transmission electron microscopy, we have visualized the decomposition chemistry of K_2PtCl_4 to identify its transient intermediate phases and their interfaces that characterize the chemical reduction process. The crystalline structure of K_2PtCl_4 is found to undergo a disproportionation reaction to form K_2PtCl_6, followed by gradual reduction to crystalline Pt metal and KCl. By directly imaging different Pt—Cl bond configurations and comparing them to models predicted via density functional theory calculations, a causal connection between the initial and final states of a chemical reaction is established, showcasing new opportunities to resolve reaction pathways through atomistic experimental visualization.

INTRODUCTION

Chemical reactions, converting reactant materials to new products, proceed by breaking and establishing bonds among atoms. The reactions described by the reagents and end products can take different pathways characterized by various intermediate products and elementary steps. Each intermediate step has its own reaction rate and energy barrier, and therefore, understanding the kinetics of each step can offer insights to control or modify the overall reaction and design new materials with desired structures and properties (*1*). By merit of the transient nature of intermediate products, the reaction pathway cannot be determined only on the basis of the beginning and ending products using ex situ methods. Instead, investigations into the existence and characterization of a chemical process' intermediate phases should be performed using an in situ method that mimics real world conditions to create a time-resolved description of the reaction (*2*, *3*). Traditionally, chemical characterization studies are performed using a combination of diffraction and spectroscopic methods to identify the intermediate products (*4*–*6*). These studies can operate at fast timescales and on large sample volumes so that short-lived transient phenomena may be captured; diffraction and spectroscopy methods can also provide time-resolved information on the order of picoseconds (*4*, *7*). However, at these large sampling volumes, events occurring at the single molecule or atomic scale can be lost to signals generated by the bulk of the material. These characterization techniques also lack imaging capabilities. Because new, functional nanomaterials require precise manipulation at the atomic scale and, more importantly, the events occurring sporadically in the local domains are often found to be the initiation of a new reaction stage, the nucleation sites of a new phase, or the cause of a catastrophic material failure (*8*–*10*), it is important to clarify chemical processes at the atomic scale using the combination of advanced imaging tools with theoretical calculation.

Aberration-corrected transmission electron microscopy (TEM) now offers to resolve static materials structures at the atomic level routinely. It is also possible to directly monitor the change in nanostructures under electron beam (*11*). The imaging electrons in TEM are capable of modifying samples through beam effects (*12*–*18*). This can often be desirable if the electron beam is intended to trigger a chemical reaction of interest. With the advancement of in situ environmental techniques to host a variety of reaction environments within the confines of TEM, in situ TEM has offered the direct visualization of the dynamic processes of nanoparticle catalyst during their growth, exposure to elevated temperatures (*19*, *20*), galvanic corrosion (*21*, *22*), and influence under surfactants (*23*, *24*). Studies have also provided insight into the dynamics of self-assembling nanomaterials (*25*, *26*). In particular, the strength of high spatial resolution of TEM for in situ experiments has been demonstrated in recent works to image solid-state chemistry, including the thermally driven growth dynamics of MoS_2 (*27*), the decomposition of halide perovskites under irradiation to form metallic nanoparticles (*28*, *29*), and the formation of NaCl crystals and metal organic frameworks (*30*–*33*). However, very few studies look at the chemical reaction pathway during the nucleation and growth of metal nanoparticles (*34*). The existing research has overwhelmingly focused on nucleation in the liquid state to most closely imitate the solution-based approaches used to form engineered nanoparticles (*35*–*37*), where individual precursor molecules and ions can hardly be visualized, because of their high mobility in

[1]Future Material Innovation Center, Zhangjiang Institute for Advanced Study, Shanghai Jiao Tong University, Shanghai 200240, P. R. China. [2]Department of Materials Science and Engineering, North Carolina State University, Raleigh, NC 27695, USA. [3]Davidson School of Chemical Engineering, Purdue University, West Lafayette, IN 47907, USA. [4]State Key Laboratory of Metal Matrix Composites, School of Materials Science and Engineering, Shanghai Jiao Tong University, Shanghai, P. R. China. [5]Center of Hydrogen Science, Shanghai Jiao Tong University, Shanghai 200240, P. R. China.
*Corresponding author. Email: gaowenpei@sjtu.edu.cn (W.G.); jianbowu@sjtu.edu.cn (J.W.); zeng46@purdue.edu (Z.Z.)
†These authors contributed equally to this work.
‡Present address: Oak Ridge National Laboratory, 1 Bethel Valley Road, Oak Ridge, TN 37830, USA.
§Present address: Protochips Inc, 3800 Gateway Centre Blvd Ste 306, Morrisville, NC 27560, USA.

liquid environment. Consequently, this frustrates efforts to record the beginning of nucleation and the chemical reduction process required to obtain neutrally charged Pt atoms with high fidelity.

Thus, it becomes necessary to adopt a solid-state approach to investigate the chemistry of Pt nanoparticle formation from its chemical precursor. In the prior effort, the solid-state decomposition dynamics of the Pt precursor K_2PtCl_4 were visually resolved using conventional TEM (CTEM) (*38*). Although the images captured the formation of Pt nanoparticles at atomic resolution, a detailed change in the Pt—Cl bonding characteristics and the presence of various intermediate phases were not available. Phase determination and evolution were performed via power spectra, which is not well suited to recognize the presence of localized structures that correspond to scarcely distributed, site-specific intermediate phases. Determining the chemical species via CTEM imaging can also be difficult because of the challenge in differentiating light and heavy elements using phase contrast. To overcome the former study's limitations, we have characterized the entire solid-state chemical processes of the Pt precursor, K_2PtCl_4, using atomic-resolution scanning TEM (STEM) in combination with density functional theory (DFT) calculation–derived models. The use of high-angle annual dark-field (HAADF) STEM is beneficial because it provides much greater contrast between light and heavy elements via Z-contrast, which is critical to recognizing the center of Pt-Cl molecule species. In addition, in conjunction with HAADF-STEM, integrated differential phase contrast (iDPC) permits the dose-efficient visualization of light elements, including Cl, C, N, O, and H, that are essential parts of a chemical species' structure and necessary to fully understanding its dynamical interactions (*39*, *40*). This set of imaging techniques has been demonstrated to be successful at efficiently capturing dynamic processes featuring a combination of light and heavy elements (*41*, *42*).

Thereby, we studied the decomposition of K_2PtCl_4, a precursor of Pt metal, and found that K_2PtCl_4 undergoes a disproportionation reaction to form K_2PtCl_6 upon exposure to a strong source of electron radiation, contradicting the past understanding that Pt forms directly from $[PtCl_4]^{2-}$. After follow-up reactions that remove K^+ and Cl^- during the reduction of Pt to lower oxidation states, $[PtCl_4]^{2-}$ emerges again and can move as a unit before Pt is lastly reduced to Pt^0 and lands on the growing Pt nanoparticle. Direct imaging of the molecular configurations carrying different Pt—Cl bonds offers the visualization of the entire reaction pathway.

RESULTS

Imaging the disproportionation reaction

We started with imaging K_2PtCl_4, which naturally forms salt crystallites as it dries on a TEM grid (*38*). K_2PtCl_4 has a mixed nature consisting of ionic and covalent bonds. The structure of K_2PtCl_4 can be simplified as an ionic compound consisting of K^+ and $[PtCl_4]^{2-}$ ions, so that the locations of the Pt and Cl atoms are codependent (*43*). The $[PtCl_4]^{2-}$ ion is a square planar complex wherein a quartet of Cl atoms are arranged coplanar around a Pt^{2+} atom via a partially covalent and ionic bond (*44*). Both the bonding between the K^+ and $[PtCl_4]^{2-}$ and the bonding within the $[PtCl_4]^{2-}$ ion can be easily broken by high-energy electrons, making K_2PtCl_4 extremely sensitive to an electron beam. Visualization of the chloroplatinate ions as they decay into their Pt^0 and Cl^- components is necessary to obtain a complete understanding of the nucleation kinetics of Pt nanoparticle from K_2PtCl_4. Using the segmented dark-field detector to perform iDPC imaging (Fig. 1A) in combination with HAADF imaging in STEM, we image K_2PtCl_4 along the [100] zone axis (Fig. 1B) with all the atomic columns including Pt, K, and Cl clearly visible and identified as shown in Fig. 1 (C and D). Sensitive to electron radiation, K_2PtCl_4 only requires a small electron dose to decompose. The delicate nature of K_2PtCl_4 is demonstrated in Fig. 2 (A to D) and movie S1. Under an electron beam, a new phase emerges within K_2PtCl_4 and proceeds to grow as the phase boundaries migrate until all of the K_2PtCl_4 is consumed. The new phase, shown in Fig. 2 (G and H), is identified as K_2PtCl_6, a typical precursor compound with the Pt oxidation of 4+. The K_2PtCl_6 hosts Pt-Cl_6 octahedra with a net charge of 2−, balanced by the two K^+ ions, as shown by the structural model in Fig. 2I. Here, the transformation of K_2PtCl_4 to K_2PtCl_6 is a consequence of a disproportionation reaction mediated by the electron beam. This disproportionation reaction merges a set of two $[PtCl_4]^{2-}$ ions into a single $[PtCl_6]^{2-}$ ion to release a neutral Pt atom and two Cl^- ions in accordance with the following stoichiometry

$$2\{2\,K^+ + [Pt(II)Cl_4]^{2-}\} \rightarrow \{2\,K^+ + [Pt(IV)Cl_6]^{2-}\} + Pt(0) + 2\,KCl \quad (1)$$

DFT calculations predict that the thermodynamic energy difference at 0 K for the disproportionation reaction is 0.05 eV/formula unit. During an electron-scattering event, the electrons usually transfer several electron volts of energy via knock-on damage or radiolysis, which easily overcomes the energy difference as well as activation barrier required to permit this reaction (*12*). Because knock-on damage can remove atoms from the sample rather than breaking the bonds between atoms, the observed decomposition process is more a result from radiolysis. As shown in Eq. 1, throughout this phase transformation, Pt atoms are free from their chloroplatinate molecules so that the Pt nanoparticle nucleation and growth can begin. The formation of Pt nuclei is random so that nucleation can occur anywhere within the irradiated volume of the precursor. In the complete HAADF and iDPC image series showing the phase transition (figs. S1 and S2 and

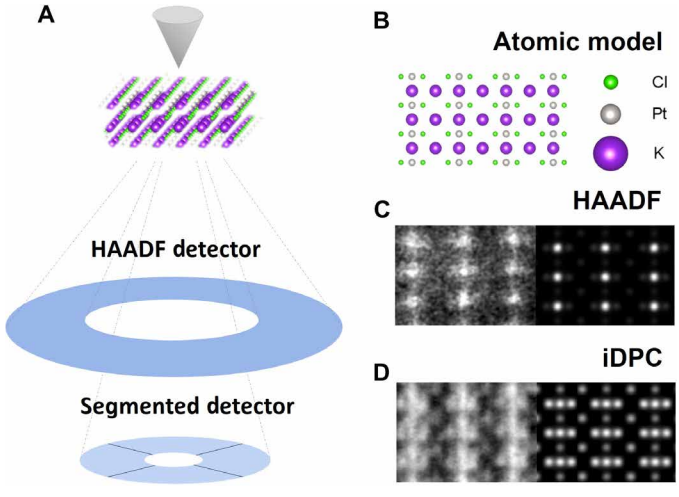

Fig. 1. TEM experimental design. (**A**) A schematic of the in situ experimental design depicting the acquisition of HAADF and iDPC images along the [100] zone axis of K_2PtCl_4. (**B**) An atomic model of K_2PtCl_4. (**C** and **D**) The experimental (left) and simulated (right) STEM images of K_2PtCl_4 as acquired via a (C) HAADF or (D) segmented detector.

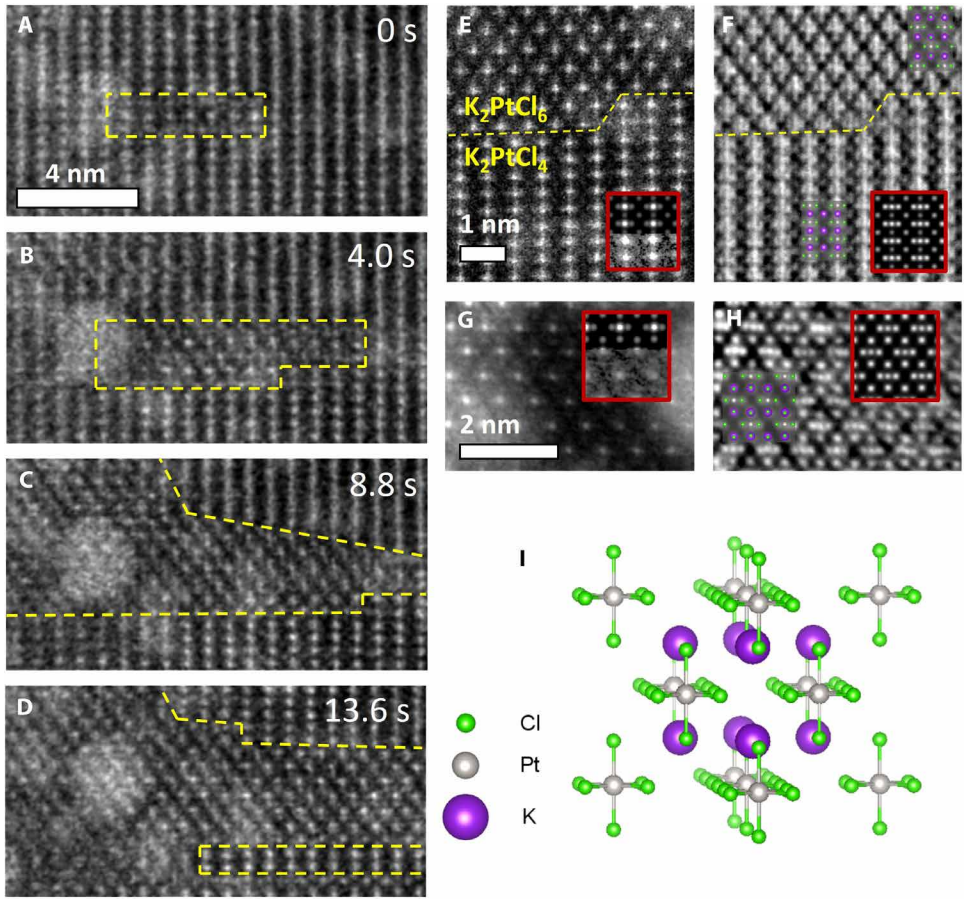

Fig. 2. The disproportionation of K_2PtCl_4 into K_2PtCl_6. (**A** to **D**) HAADF-STEM image series capturing the disproportionation of K_2PtCl_4 into K_2PtCl_6. The interface between the phases is outlined. Each frame is acquired over roughly 0.8 s with an electron dose of approximately 900 $e^-/Å^2$. (**E** and **F**) Experimental (E) HAADF and (F) iDPC STEM images of the interface between K_2PtCl_4 and K_2PtCl_6 along the [100] zone axis of K_2PtCl_4. Images acquired with an electron dose of approximately 3600 $e^-/Å^2$. Simulated images are provided in insets, and the atomic models are overlaid. (**G** and **H**) Experimental (G) HAADF and (H) iDPC images of K_2PtCl_6 along the [110] zone axis. Simulated images are provided in insets, and an atomic model is overlaid. The images are composed of 10 aligned frames for a total electron dose of approximately 36,000 $e^-/Å^2$. (**I**) Atomic model of K_2PtCl_6.

movie S1), the boundary between K_2PtCl_4 and K_2PtCl_6 (Fig. 2, E and F) is abrupt without an amorphous transition region. The benefit of using a combination of HAADF and iDPC is demonstrated in these images: The Z-contrast provided by HAADF has allowed for the easy identification of the Pt atom at the center of the chloroplatinate ions; the iDPC has provided the location of the faint Cl and K columns. Unlike the parent phase, the intermediate product, K_2PtCl_6, may sustain higher electron dose, and the image can have a higher signal-to-noise ratio, as demonstrated in Fig. 2 (G and H). The existence of K_2PtCl_6, and its interface with K_2PtCl_4 has also been confirmed through the careful analysis of atomic-resolution images taken from multiple zone axes (fig. S3). Beyond matching the apparent plan view appearance of the images to the theoretical phase (*45*), measurements of the K_2PtCl_6 lattice parameters along the [110] and [310] zone axes have been obtained, as presented in table S1 (*46*).

The disproportionation reaction involves the redistribution of charge between the two Pt atoms. This proposed radiation induced chemical reaction path explains the radiation sensitivity of K_2PtCl_4 and more durable nature of K_2PtCl_6. Pt does not typically adopt higher charges than a Pt^{4+} state, so degradation beyond this point will generally rely on severing the Pt—Cl bonds. This phase change also results in a new crystalline symmetry; K_2PtCl_6 is part of the $Fm\bar{3}m$ space group rather than the $P4/mmm$ space group of K_2PtCl_4. K_2PtCl_6 has a lattice parameter expansion along C compared to K_2PtCl_4. The presence of this reaction explains the source of the free Pt atoms involved in the initial nucleation of Pt nanoparticles.

Bond breaking in K_2PtCl_6

Shown in movies S2 and S3 and figs. S4 and S5, during the reduction of K_2PtCl_6, a comparably slow process principally dependent on the severing of Pt—Cl bonds, the positions of Pt and Cl atoms in K_2PtCl_6 show variations in the Pt—Cl bond angles. The initial and modified bond configurations are demonstrated in Fig. 3 (A and B). The evolution of the representative bond angles is presented in a time series (fig. S6). To relate the bond angle change in experiments with the removal of Cl and K atoms or a pair of K-Cl atoms, we modeled the local lattice distortions associated with the removal of atoms from the exposed (*101*) surface of K_2PtCl_6 using DFT. The DFT relaxed structures and their associated iDPC image simulations for can be found in figs. S7 to S9.

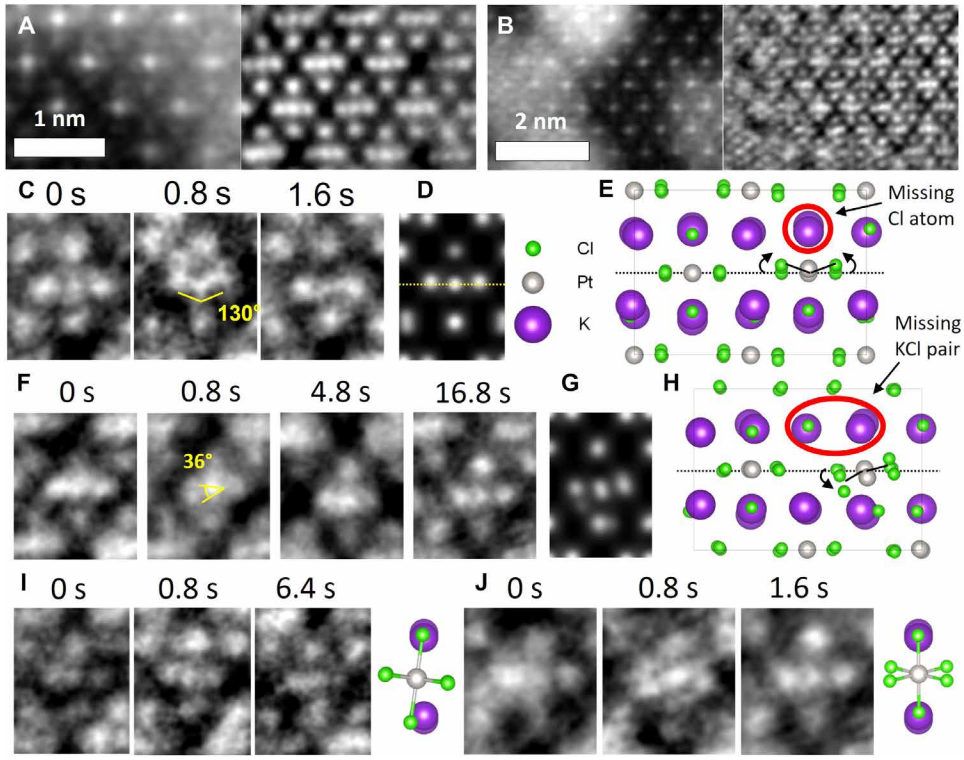

Fig. 3. The reduction of K_2PtCl_6. (**A** and **B**) HAADF (left) and iDPC (right) STEM images demonstrating the decomposition of K_2PtCl_6 along its [110] zone axis. Each image is an aligned and summed series of 10 frames acquired over roughly 0.8 s with an electron dose of approximately 3600 $e^-/Å^2$ per frame. (**C**) An iDPC image series of a $[PtCl_6]^{2-}$ molecule losing a single Cl atom. (**D** and **E**) The (D) iDPC simulation and (E) atomic model of the DFT-derived structure of K_2PtCl_6 with a missing Cl atom in the plane perpendicular position. (**F**) An iDPC image series of K_2PtCl_6 losing a KCl pair. (**G** and **H**) The (G) iDPC simulation and (H) atomic model of the DFT-derived structure of K_2PtCl_6 with a missing KCl pair. A Gaussian blur has been applied to the single-molecule iDPC series. (**I**) iDPC series and (**J**) atomic models depicting the rotation of a $PtCl_6$ molecule to show its additional Cl atom sites.

In experiments, the bond angle change is measured by the deviation of Cl and Pt atom positions from the coplanar Cl—Pt—Cl bonds along the equator of the $[PtCl_6]^{2-}$ octahedra. In Fig. 3C, the Cl—Pt—Cl bonds across the equatorial plane appear to be bowing, with the Cl—Pt—Cl bond angle measured to be between ~130° and 135°. From the DFT results, this change results from the removal of a single neutral Cl atom from the $PtCl_6$ octahedra, documented in Fig. 3E and fig. S7. In Fig. 3D, the simulated HAADF-STEM image of the atomic structure model matches closely with the experimental image. In this instance, the Cl atom is removed from the plane perpendicular position. DFT calculations find that this mode of decomposition results in the reduction of the Pt atom into a 3+ state because the Cl is cleaved as a radical in DFT calculations. If the Cl atom is removed from the Pt-Cl_4 equatorial plane, then DFT predicts no disturbance to the Cl—Pt—Cl bond angle. DFT calculations do not predict a preferential Cl removal site. The energy required to remove Cl from equatorial or plane perpendicular position is almost the same ($\Delta E < 1$ meV/Å^2). Similarly, the energy required to removal a Cl atom from the surface is not meaningfully distinct from the bulk. Hence, along the [110] zone axis of K_2PtCl_6, this mode can only be detected when an out-of-plane Cl atom is removed. Experimental observations demonstrate that the $[PtCl_5]^{2-}$ molecule is a transient state. In both example series (fig. S10, A and B), the symmetry break is only present for a single frame before adopting an appearance similar to a typical $[PtCl_6]^{2-}$ octahedra. This transient behavior is confirmed by DFT, which predicts that the energy required to further reduce the molecule to $[PtCl_4]^{2-}$ is negligible compared to the energy required to remove the first Cl ($\Delta E < 1$ meV/Å^2).

In Fig. 3F, the image captures a splitting in the Cl column with two distinct peaks emerging at a ~36° angle from the central Pt atom. On the basis of the DFT-calculated structure, this more asymmetric appearance results from the decomposition path where the K^+ and Cl^- ion pair is removed (Fig. 3H). Figure 3G shows the simulated HAADF-STEM image based on the atomic model. With a Cl atom missing in the plane perpendicular position, the $[PtCl_5]^-$ molecule rotates away from the missing K^+ ion. This process does not change the Pt oxidation state from 4+. The remaining planar perpendicular Cl atom is also expected to be tilted away from the original axis, but this is difficult to observe along the [110] zone axis of K_2PtCl_6 because of the plane perpendicular site's overlap with the K columns. A DFT structure for the removal of a Cl atom in a Pt-Cl_4 equatorial plane and an adjacent K atom is available in fig. S8. This configuration is predicted to tilt the apparent molecular equatorial plane with asymmetric Cl column broadening.

It is experimentally challenging to identify the removal of two Cl atoms from the $[PtCl_6]^{2-}$ octahedra. On the basis of DFT calculations, removing two Cl atoms will result in the formation of a $[PtCl_4]^{2-}$ molecule, bringing the Pt atom to a 2+ charge state. If the Cl atoms are taken from the plane perpendicular positions, then the resulting square planar $PtCl_4$ structure is expected to be experimentally

identical to an octahedral $PtCl_6$ molecule without introducing substantial lattice distortions (see fig. S9). Alternative Cl atom removal sites can be considered, but the square planar configuration is the most stable. In the event two Cl atoms were removed from the equatorial plane, the remaining Cl atoms within the plane would appear to be slightly further from the Pt atom.

Therefore, from both experiments and DFT calculation, three paths of Cl atom removal are visualized and described: (i) the removal of a neutral Cl atom, (ii) the removal of a K^+ and Cl^- ion pair, and (iii) the removal of two Cl atoms. The visual appearance of the $PtCl_{6-x}$ molecule in the paths depends on its local K^+ cage and the missing Cl atom sites; specifically, the Cl atom(s) can be missing from the Pt-Cl_4 equatorial plane or the perpendicular out-of-plane sites.

Note that experimental images and DFT calculations indicate that the $[PtCl_6]^{2-}$ octahedra are initially disrupted by the severing of Pt—Cl bonds to form a $[PtCl_5]^{x-}$ ($x = 1, 2$) intermediate product, wherein the decomposition mode and Pt charge state are visually determinable by localized molecular distortions. The removal of an additional Cl atom is expected to result in the formation of square planar $[PtCl_4]^{2-}$ molecules that will appear indistinguishable from any neighboring $[PtCl_6]^{2-}$ molecules. The presence of multiple $[PtCl_4]^{2-}$ molecules within the lattice presents the possibility of a cyclic disproportionation process. If these molecules are adjacent to each other, then they could react to produce a $[PtCl_6]^{2-}$ molecule. DFT calculations have compared the energy favorability of cyclic disproportionation to radiolysis. Under ambient conditions, there is a strong preference for disproportionation over radiolysis (fig. S11). Consequently, it is unlikely that any chloroplatinate molecules with fewer than four Cl bonds will be observed until the disproportionation process is no longer possible. This event becomes likely once the remaining molecules have become rarified. The disruption of the local K_2PtCl_6 configuration also causes changes of the lattice nearby; $[PtCl_6]^{2-}$ can move and rotate. Figure 3 (I and J) shows the rotation of $[PtCl_6]^{2-}$ captured by the atomic-resolution images.

These insights into the chemical decomposition of K_2PtCl_6 permit the description of a cyclic disproportionation process that expedites the release of Pt atoms without the need for $PtCl_x$ ($x = 1, 2, 3$) intermediate products. Hence, few, if any, free Pt atoms are produced directly through the random severing of Pt—Cl bonds. Rather, the loss of Cl atoms permits a $[PtCl_6]^{2-}$ molecule to be converted into $[PtCl_5]^{x-}$ ($x = 1, 2$) and eventually $[PtCl_4]^{2-}$. Once two nearby $[PtCl_4]^{2-}$ molecules are created, they can be consumed in the disproportionation reaction, thereby liberating a Pt atom. These Pt atoms may then join an existing Pt nanoparticle through a diffusion process. The KCl generated throughout this process is similarly sequestered to planar KCl sheets nucleated on the surface of the K_2PtCl_6 precursor (see fig. S12 to S15 and the Supplementary Materials for additional information). The majority of the K_2PtCl_6 reduction process can therefore be described using the following set of stoichiometries

$$2\ [Pt(IV)Cl_6]^{2-} \rightarrow 2\ [Pt(III)Cl_5]^{2-} + Cl_2(g) \quad (2)$$

$$2\ [Pt(III)Cl_5]^{2-} \rightarrow 2\ [Pt(II)Cl_4]^{2-} + Cl_2(g) \quad (3)$$

$$2\{2\ K^+ + [Pt(II)Cl_4]^{2-}\} \rightarrow \{2\ K^+ + [Pt(IV)Cl_6]^{2-}\} + Pt(0) + 2\ KCl \quad (4)$$

The Pt nucleation

The solid-state reduction dynamics of K_2PtCl_4 are responsible for controlling the nucleation and growth kinetics of the resulting Pt nanoparticles. These dynamics result in three separate rates of Pt release from the precursor. The first regime is the initial release of Pt when the pristine K_2PtCl_4 precursor undergoes a fast disproportionation reaction to produce K_2PtCl_6. From stoichiometry, it is expected that a full half of the potential Pt atoms are made available to form Pt nuclei in this first stage. This process was directly captured in movie S1. Figure 4 (A to C) provides a demonstration of the events immediately following Pt nucleation. In Fig. 4A, the disproportionation reaction has just completed to leave behind a cluster of small Pt nuclei roughly 1 nm in diameter. As the reaction proceeds in Fig. 4 (B and C), the nuclei coalesce to form a single Pt nanoparticle. The coalescence of nanoparticles has no particular orientation preference, and nanoparticles can easily reorient themselves as they expand.

The second kinetics regime is the cyclic disproportionation process that gradually removes Pt from K_2PtCl_6. The limited concentration of $[PtCl_4]^{2-}$ ions limits the Pt release rate. Consequentially, Pt nucleation is not typical. Instead, the existing Pt nanoparticles will capture the newly released Pt and grow until the nearby K_2PtCl_6 precursor is exhausted. This process is shown in Fig. 4 (D to G). Starting from Fig. 4D, crystalline K_2PtCl_6 can be found adjacent to a Pt nanoparticle. By comparing the HAADF and iDPC images, it is

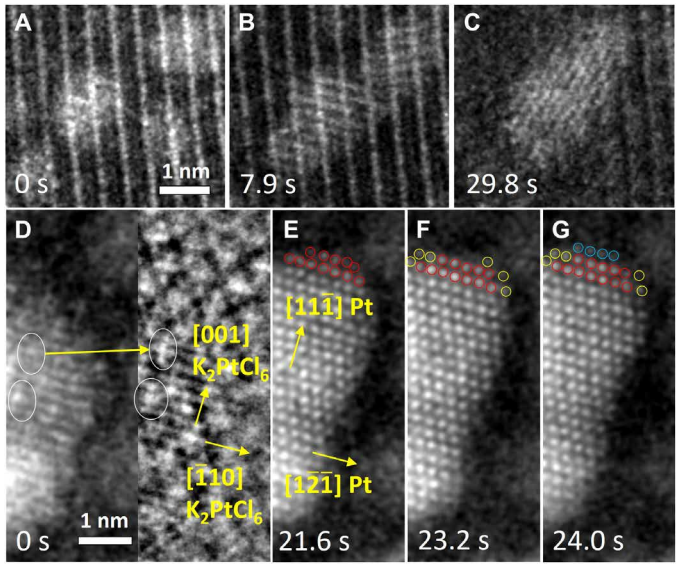

Fig. 4. The growth kinetics of Pt nanoparticle during K_2PtCl_4 reduction. (**A** to **C**) The rapid disproportionation of K_2PtCl_4 results in fast Pt nucleation and coalescence kinetics demonstrated via HAADF-STEM images acquired along the [120] zone axis of K_2PtCl_6. Each frame is acquired over roughly 1.6 s with an electron dose of approximately 7200 $e^-/Å^2$. (A) The initial Pt nuclei shortly after the beginning of disproportionation reaction. (B) and (C) The coalescence of small Pt nuclei into a single nanoparticle. (**D** to **G**) The cyclic disproportionation and eventual rarified reduction of K_2PtCl_6 result in slow Pt nanoparticle growth kinetics so that the nanoparticle can be seen growing on an atom-by-atom basis. Each frame is acquired over roughly 0.8 s with an electron dose of approximately 3600 $e^-/Å^2$. (D) HAADF (left) and iDPC (right) images demonstrating a Pt nanoparticle coincident against the [110] zone axis K_2PtCl_6 precursor. The $[PtCl_6]^{2-}$ ions are circled for emphasis. (E) to (G) Without the nearby K_2PtCl_6 lattice, the nanoparticle grows slowly by absorbing rarified Pt metal atoms.

apparent that the K_2PtCl_6 precursor lattice overlaps the Pt nanoparticle. As the precursor is reduced, the Pt nanoparticle grows substantially and gradually over time.

If there is a directional bias in the flow of Pt atoms, the adjoining Pt atoms on the nanoparticle surface can follow a kinetically controlled layer-by-layer growth process. In Fig. 4 (D to G), such a process leads to the anisotropic growth along Pt <111>, so the Pt nanoparticle adopts a nanorod morphology. Although there is no universal orientation relationship between Pt and K_2PtCl_6 in all regions, the nanoparticle in Fig. 4D and precursor lattice are aligned, so that the nanoparticle grows along its $[\bar{1}11]$ direction and follows $([\bar{1}10]_{K_2PtCl_6} \parallel [\bar{1}2\bar{1}]_{Pt}) \perp ([001]_{K_2PtCl_6} \parallel [11\bar{1}]_{Pt})$. It should be emphasized that the formation of a crystallographic relationship between the burgeoning Pt nanoparticles and degrading K_2PtCl_6 lattice is not a consistent feature, but specific orientation relationships may influence the growth trajectory of Pt nanostructures. A similar orientation relationship exists between K_2PtCl_6 and KCl, which causes the KCl to adopt a planar sheet morphology (see figs. S12 to S15).

The final kinetics regime of Pt nanoparticle growth occurs once the crystalline precursor is exhausted and only rarified $PtCl_x$ molecules remain. Because of the much higher distance between $PtCl_x$ molecules at this point, Pt atom release is unlikely to occur though a disproportionation process. Instead, the various $PtCl_x$, $x = (1, 2, 3)$, states will need to be reduced through the gradual severing of bonds. This will result in further Pt nanoparticle growth after the K_2PtCl_6 precursor lattice is depleted. If this final stage is not completed, then Pt-Cl molecules are expected to migrate as adatoms on the nanoparticle surfaces.

DISCUSSION

In this study, by expanding the imaging capability of electron microscopy to the investigation of intermediate products in solid-state chemical reactions, the electron radiation induced chemical reduction of K_2PtCl_4 has been successfully visualized. This chemical reaction and its associated Pt release kinetics have been summarized in Fig. 5. Initially, the precursor exists as pure K_2PtCl_4. Under electron beam irradiation, the $[PtCl_4]^{2-}$ ions will disproportionate into $[PtCl_6]^{2-}$ and release neutral Pt atoms and K^+ and Cl^- ion pairs. The Pt atoms will quickly form the initial Pt nuclei. As disproportionation completes, the Pt nuclei will coalesce to form nanoparticles while the K^+ and Cl^- ions find favorable sites on the K_2PtCl_6 lattice to form a planar sheet of KCl. Once the initial K_2PtCl_4 precursor chemical is expended, the precursor lattice will have been converted to K_2PtCl_6 that is subsequently reduced through a cyclic process of disproportionation. As this occurs, the $[PtCl_6]^{2-}$ ions will be reduced into a transient $[PtCl_5]^{1,2-}$ molecule before further reduction to $[PtCl_4]^{2-}$. In this intermediary stage, the asymmetrical Pt—Cl bond configurations, deviating from the initial $[PtCl_6]^{2-}$ octahedra, are captured by atomic-resolution STEM imaging. Upon the creation of multiple nearby $[PtCl_4]^{2-}$ ions, the disproportionation reaction will occur to reset the cycle and grow the Pt nanoparticles and KCl lattice. This will continue until the K_2PtCl_6 lattice is almost completely depleted, until there are no remaining densely populated regions. As the precursor becomes rarified and incapable of undergoing disproportionation, large Pt nanoparticles with $PtCl_x$ adatoms will have formed. Once the reaction is complete, the Pt nanoparticle surfaces will be free of Pt-Cl adatoms.

The observations in this work may be compared against previous studies in the literature performed using conventional techniques. Historically, the decomposition of K_2PtCl_4 has been studied using spectroscopic methods (*47*, *48*). In an aqueous pulse radiolysis study, the reduction of $[PtCl_4]^{2-}$ was described as a complex process that transitions through unstable Pt (I) and (III) oxidation states that terminate through disproportionation reactions before eventually obtaining Pt(0) (*48*). Conversion to an odd oxidation state was believed to be mediated by OH, H, or e^- radicals within the solution. This confirms that disproportionation reactions are expected to be a typical feature in the chemical reduction of chloroplatinate molecules. However, the presence of radicals within the aqueous solution are involved in the process. The most directly comparable experiment to this study has been an investigation of the effect of gamma radiation on solid-state K_2PtCl_4 using electron spin resonance spectroscopy (*47*). Although the spectroscopic study did not provide a complete description of the chemical reduction process, it did critically confirm the existence of a transient Pt (III) state in the absence of solution-derived radicals. In addition, it showed that Cl atoms removed via radiolysis can be charge neutral. Together, these studies demonstrate that the oxidation of Pt^{4+} to produce a K_2PtCl_6 intermediate phase through a disproportion reaction occurs in the chemical reduction of K_2PtCl_4.

Note that for in situ electron microscopy studies, electron beam–induced sample damage can hide the real dynamics of a chemical reaction. Thus, care must be taken when investigating chemical reactions via in situ TEM. For the process presented in this work, it is abundantly clear that high-energy radiation can trigger the decomposition of K_2PtCl_4 (*47*–*49*). However, the nature of this decomposition may vary depending on the precursor's environment and the mediating radiation. It is generally known that the electron beam is capable of severing chloride bonds (*50*,*51*). In this work, the primary decomposition mechanisms associated with electron radiation that

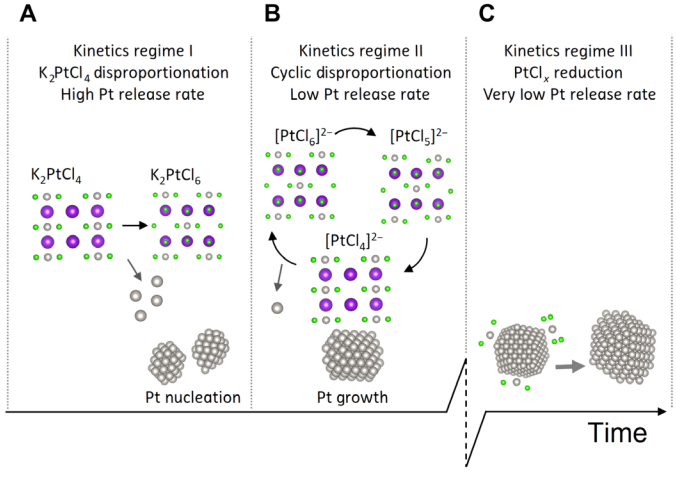

Fig. 5. The decomposition dynamics of K_2PtCl_4 and the corresponding Pt nucleation and growth kinetics. (**A**) The radiation-driven reduction of K_2PtCl_4 begins by converting K_2PtCl_4 to K_2PtCl_6 through a disproportionation process. The rapid release of neutral Pt atoms causes substantial Pt nanoparticle nucleation. (**B**) The reduction of K_2PtCl_6 principally proceeds through a cyclic disproportionation process. Electron radiolysis breaks the $PtCl_6$ molecules into $PtCl_5$ and $PtCl_4$. If sufficient $PtCl_4$ is available, then it preferentially undergoes a disproportionation reaction instead of proceeding to $PtCl_3$. This process causes the slow release of neutral Pt that grows the existing Pt nanoparticles. (**C**) At the end of the reaction, any rarified $PtCl_x$ molecules are reduced through electron radiolysis.

are considered include knock-on damage and radiolysis (*12, 52*). Knock-on damage directly removes an atom from the lattice through physical displacement. This process is dependent on the maximum energy transferred to the given atom and varies by species (*12*). For Cl, K, and Pt, this is 14.8, 13.4, and 2.7 eV, respectively, for 200-keV electrons. The considerable mass difference between Cl, K, and Pt indicates that knock-on damage will most frequently affect the Cl and K atoms. Alternatively, the electron beam may also promote and expel electrons within the atoms thereby breaking bonds through the process of radiolysis. For a semiconductor such as K_2PtCl_4, these electrons could come from either the valence or inner-shell electrons (*52*). Valence electrons can be promoted into the conduction band, resulting in the severing of atomic bonds with the energy transfer of only a few electron volts. Conversely, expelling the inner-shell electrons requires far more energy (typically on the order of at least hundreds of electron volts). It is known from ultraviolet radiation synthesis that K_2PtCl_4 requires at least a minimum wavelength of 420 nm to decompose without a catalyst, corresponding to a ~3 eV or greater barrier to photoreduction (*49*). This barrier is quite easily bridged via the electron beam, which could demonstrate a possible similarity between the two forms of radiative decomposition.

The utilization of both HAADF-STEM and iDPC has proven instrumental in completely characterizing the reduction chemistry of K_2PtCl_4 beyond what was accomplished in the prior work (*38*). The Z-contrast provided by HAADF was the first and clearest indication of the nature of the K_2PtCl_4 to K_2PtCl_6 phase transition by unambiguously differentiating the Pt columns from the K and Cl. Furthermore, the iDPC was also necessary to image light elements so that the varying Pt—Cl bond angles could be resolved. The utilization of phase contrast alone can lead to ambiguity in complex transient regions or alone certain zone axes such as the [001] of K_2PtCl_4, wherein the structural changes are less easily observed. By using both image formation mechanisms and comparing the resulting images, it was possible to observe and describe the initial, intermediate, and ending chemicals in a reaction at the atomic level. The method developed in this work can easily be translated to study more complex solid-state reactions.

MATERIALS AND METHODS

Materials and sample preparation

To prepare the TEM sample of crystalline K_2PtCl_4, powdered K_2PtCl_4 was dissolved in deionized water and drop casted onto a 3-mm holey carbon TEM grid. The drop of solution coating the grid was then allowed to dry in air to promote effective crystallization.

TEM image methods

All TEM experiments in this in situ study were performed on an aberration-corrected FEI Titan scanning transmission electron microscope operated at 200 kV. STEM images are taken using a semiconvergence angle of 17.9 mrad at an electron current of approximately 10 pA. Images were acquired within the FEI Velox suite using a combination of the HAADF and a four-segment annular dark field (ADF) detector. The segmented ADF data were recorded as a set of images corresponding to the difference between opposite segments. These data were then used to create iDPC images in accordance with the theory described by Lazic (*39*). The microscope was configured so that the HAADF and DF4 detectors covered a range of 39 to 200 and 9 to 36 mrad, respectively.

Data processing and STEM image simulation

Various forms of image processing have been used to improve the interpretability and clarity of the data. All iDPC images have been processed through a high-pass Fourier filter to eliminate noise. A Gaussian filter has been applied to all HAADF images unless otherwise noted in figure legend text. In addition, the image series have been aligned to permit the combination of multiple images to improve the signal-to-noise ratio (*53*).

Multislice simulation of STEM image were carried out using Dr. Probe with the parameters adjusted according to the experimental settings of acceleration voltage, probe convergence angle, and detector collection angles. One hundred frozen phonon configurations were used (*54*). The iDPC simulations of the DFT relaxed structures depicted in figs. S7 to S9 were performed in the following manner. As appropriate, the K and Cl atoms were removed from the surface of the structure before DFT relaxation. A pristine layer of K_2PtCl_6 exists beneath the modified layer with the removed atom(s). iDPC simulations were performed with and without the inclusion of the pristine K_2PtCl_6 layer. The layers included in each iDPC simulation are denoted in figs. S7 to S9 along with atomic models showing the top and side views of the structure, which also highlight the location of the missing atoms. Every layer of the structure considered in the simulations is 7 Å thick.

DFT calculations

The DFT calculations were performed using Vienna Ab Initio Simulation Package (VASP) (*55*, *56*). The core electrons were modeled using projector augmented wave potentials (*57*). The Perdew-Burke-Ernzerhof functional, which is a form of generalized gradient approximation was used, and the energy cutoff of the planewave basis were set to 500 eV (*58*). The Monkhorst-Pack k point scheme was used for all the calculations. The bulk unit cells for Pt, KCl, K_2PtCl_4, and K_2PtCl_6 were obtained from the Materials Project database (*59*). The relaxed K_2PtCl_6 bulk unit cell was cut along the (101) direction to make a four-layer-thick slab. Each unit cell was initially comprised of eight $PtCl_6$ molecules and their associated K^+ cations. The defects were created by removing Cl, Cl_2 and KCl units from the surface, and all the possible structures were exhaustively numerated. For each defect condition, Cl atoms are only removed from a single $PtCl_6$ molecule on the (101) surface plane. The oxidation state of Pt was determined using Bader charge analysis described by Henkelman *et al.* (*60*) The Bader charge values of slab structure were normalized using Bader charges of bulk compounds with known oxidation states.

Supplementary Materials

This PDF file includes:

Supplementary Text
Figs. S1 to S15
Table S1
Legends for movies S1 to S3

Other Supplementary Material for this manuscript includes the following:

Movies S1 to S3

REFERENCES AND NOTES

1. T. S. Rodrigues, M. Zhao, T.-H. Yang, K. D. Gilroy, A. G. M. da Silva, P. H. C. Camargo, Y. Xia, of colloidal metal nanocrystals: A comprehensive review on the reductants. *Chem. A Eur. J.* **24**, 16944–16963 (2018).

2. S. Jeon, T. Heo, S.-Y. Hwang, J. Ciston, K. C. Bustillo, B. W. Reed, J. Ham, S. Kang, S. Kim, J. Lim, K. Lim, J. S. Kim, M.-H. Kang, R. S. Bloom, S. Hong, K. Kim, A. Zettl, W. Y. Kim, P. Ercius, J. Park, W. C. Lee, Reversible disorder-order transitions in atomic crystal nucleation. *Science* **371**, 498–503 (2021).
3. C. F. Reboul, J. Heo, C. Machello, S. Kiesewetter, B. H. Kim, S. Kim, D. Elmlund, P. Ercius, J. Park, H. Elmlund, SINGLE: Atomic-resolution structure identification of nanocrystals by graphene liquid cell EM. *Sci. Adv.* **7**, eabe6679 (2021).
4. I. V. Tomov, P. Chen, P. M. Rentzepis, Picosecond time-resolved X-ray diffraction during laser-pulse heating of an Au(111) crystal. *J. Appl. Cryst.* **28**, 358–362 (1995).
5. T. Krigas, M. T. Rogers, ESR Study of Radicals Formed by γ Irradiation of K_2 $PdCl_4$ and $(NH_4)_2$ $PdCl_4$ Single Crystals. *J. Chem. Phys.* **54**, 4769–4775 (1971).
6. Z. Huang, M. Bartels, R. Xu, M. Osterhoff, S. Kalbfleisch, M. Sprung, A. Suzuki, Y. Takahashi, T. N. Blanton, T. Salditt, J. Miao, Grain rotation and lattice deformation during photoinduced chemical reactions revealed by in situ X-ray nanodiffraction. *Nat. Mater.* **14**, 691–695 (2015).
7. K. H. Kim, J. G. Kim, S. Nozawa, T. Sato, K. Y. Oang, T. W. Kim, H. Ki, J. Jo, S. Park, C. Song, T. Sato, K. Ogawa, T. Togashi, K. Tono, M. Yabashi, T. Ishikawa, J. Kim, R. Ryoo, J. Kim, H. Ihee, S. Adachi, Direct observation of bond formation in solution with femtosecond X-ray scattering. *Nature* **518**, 385–389 (2015).
8. Y. Zhang, Z. Zhang, W. Liu, L. Li, H. Jin, Y. Zheng, J. Su, N. Liu, Y. Gao, In situ TEM investigations on the controlled phase transformation of vertically aligned WS2 at designated locations on an atomic scale. *J. Phys. Chem. C.* **125**, 2761–2769 (2021).
9. O. Dyck, M. Ziatdinov, D. B. Lingerfelt, R. R. Unocic, B. M. Hudak, A. R. Lupini, S. Jesse, S. V. Kalinin, Atom-by-atom fabrication with electron beams. *Nat. Rev. Mater.* **4**, 497–507 (2019).
10. X. Chen, J. Wang, X. Sun, D. Zakharov, S. Hwang, G. Zhou, In-situ atomic-scale visualization of atomic-step induced NiO growth during the oxidation of ni. *Microsc. Microanal.* **27**, 1958–1959 (2021).
11. K. A. Unocic, S. C. Purdy, L. F. Allard, G. B. Collinge, J. Zhang, S. N. Borate, Q. Wu, E. C. Wegener, N. "River" Samad, S. Habas, T. R. Krause, J. W. Harris, M.-S. Lee, V. A. Glezakou, R. Rousseau, A. D. Sutton, Z. Li, Investigation of cu species in dealuminated beta zeolite studied by operando closed-cell gas reaction STEM. *Microsc. Microanal.* **29**, 1614–1615 (2023).
12. R. F. Egerton, P. Li, M. Malac, Radiation damage in the TEM and SEM. *Micron* **35**, 399–409 (2004).
13. S. T. Skowron, T. W. Chamberlain, J. Biskupek, U. Kaiser, E. Besley, A. N. Khlobystov, Chemical reactions of molecules promoted and simultaneously imaged by the electron beam in transmission electron microscopy. *Acc. Chem. Res.* **50**, 1797–1807 (2017).
14. J. W. Jordan, K. L. Y. Fung, S. T. Skowron, C. S. Allen, J. Biskupek, G. N. Newton, U. Kaiser, A. N. Khlobystov, Single-molecule imaging and kinetic analysis of intermolecular polyoxometalate reactions. *Chem. Sci.* **12**, 7377–7387 (2021).
15. T. W. Chamberlain, J. Biskupek, S. T. Skowron, A. V. Markevich, S. Kurasch, O. Reimer, K. E. Walker, G. A. Rance, X. Feng, K. Müllen, A. Turchanin, M. A. Lebedeva, A. G. Majouga, V. G. Nenajdenko, U. Kaiser, E. Besley, A. N. Khlobystov, Stop-frame filming and discovery of reactions at the single-molecule level by transmission electron microscopy. *ACS Nano* **11**, 2509–2520 (2017).
16. M. Tripathi, A. Mittelberger, N. A. Pike, C. Mangler, J. C. Meyer, M. J. Verstraete, J. Kotakoski, T. Susi, Electron-beam manipulation of silicon dopants in graphene. *Nano Lett.* **18**, 5319–5323 (2018).
17. R. Mirzayev, K. Mustonen, M. R. A. Monazam, A. Mittelberger, T. J. Pennycook, C. Mangler, T. Susi, J. Kotakoski, J. C. Meyer, Buckyball sandwiches. *Sci. Adv.* **3**, e1700176 (2017).
18. E. Hernández, V. Meunier, B. W. Smith, R. Rurali, H. Terrones, M. Buongiorno Nardelli, M. Terrones, D. E. Luzzi, J.-C. Charlier, Fullerene coalescence in nanopeapods: A path to novel tubular carbon. *Nano Lett.* **3**, 1037–1042 (2003).
19. W. Gao, J. Wu, A. Yoon, P. Lu, L. Qi, J. Wen, D. J. Miller, J. C. Mabon, W. L. Wilson, H. Yang, J.-M. Zuo, Dynamics of transformation from platinum icosahedral nanoparticles to larger fcc crystal at millisecond time resolution. *Sci. Rep.* **7**, 17243 (2017).
20. X. Zhang, J. Meng, B. Zhu, J. Yu, S. Zou, Z. Zhang, Y. Gao, Y. Wang, In situ TEM studies of the shape evolution of Pd nanocrystals under oxygen and hydrogen environments at atmospheric pressure. *Chem. Commun.* **53**, 13213–13216 (2017).
21. S. F. Tan, G. Lin, M. Bosman, U. Mirsaidov, C. A. Nijhuis, Real-time dynamics of galvanic replacement reactions of silver nanocubes and au studied by liquid-cell transmission electron microscopy. *ACS Nano* **10**, 7689–7695 (2016).
22. H. Shan, W. Gao, Y. Xiong, F. Shi, Y. Yan, Y. Ma, W. Shang, P. Tao, C. Song, T. Deng, H. Zhang, D. Yang, X. Pan, J. Wu, Nanoscale kinetics of asymmetrical corrosion in core-shell nanoparticles. *Nat. Commun.* **9**, 1011 (2018).
23. S. F. Tan, S. W. Chee, G. Lin, M. Bosman, M. Lin, U. Mirsaidov, C. A. Nijhuis, Real-time imaging of the formation of au–ag core–shell nanoparticles. *J. Am. Chem. Soc.* **138**, 5190–5193 (2016).
24. W. Gao, Y. Hou, Z. D. Hood, X. Wang, K. More, R. Wu, Y. Xia, X. Pan, M. Chi, Direct in situ observation and analysis of the formation of palladium nanocrystals with high-index facets. *Nano Lett.* **18**, 7004–7013 (2018).
25. Y. Liu, X.-M. Lin, Y. Sun, T. Rajh, In situ visualization of self-assembly of charged gold nanoparticles. *J. Am. Chem. Soc.* **135**, 3764–3767 (2013).
26. S. F. Tan, S. W. Chee, G. Lin, U. Mirsaidov, Direct observation of interactions between nanoparticles and nanoparticle self-assembly in solution. *Acc. Chem. Res.* **50**, 1303–1312 (2017).
27. N. Kondekar, M. G. Boebinger, M. Tian, M. H. Kirmani, M. T. McDowell, The effect of nickel on MoS_2 growth revealed with in situ transmission electron microscopy. *ACS Nano* **13**, 7117–7126 (2019).
28. J. He, Z. Liu, Z. Cao, H. Zhang, Y. Meng, B. Chen, D. Zhong, Visualizing the redox reaction dynamics of perovskite nanocrystals in real and reciprocal space. *J. Phys. Chem. Lett.* **11**, 2550–2558 (2020).
29. M. U. Rothmann, J. S. Kim, J. Borchert, K. B. Lohmann, C. M. O'Leary, A. A. Sheader, L. Clark, H. J. Snaith, M. B. Johnston, P. D. Nellist, L. M. Herz, Atomic-scale microstructure of metal halide perovskite. *Science* **370**, (2020).
30. T. Nakamuro, M. Sakakibara, H. Nada, K. Harano, E. Nakamura, Capturing the moment of emergence of crystal nucleus from disorder. *J. Am. Chem. Soc.* **143**, 1763–1767 (2021).
31. Y. Kratish, T. Nakamuro, Y. Liu, J. Li, I. Tomotsuka, K. Harano, E. Nakamura, T. J. Marks, Synthesis and characterization of a well-defined carbon nanohorn-supported molybdenum dioxo catalyst by SMART-EM imaging. surface structure at the atomic level. *Bull. Chem. Soc. Jpn.* **94**, 427–432 (2021).
32. J. Xing, L. Schweighauser, S. Okada, K. Harano, E. Nakamura, Atomistic structures and dynamics of prenucleation clusters in MOF-2 and MOF-5 syntheses. *Nat. Commun.* **10**, 3608 (2019).
33. E. Nakamura, Atomic-resolution transmission electron microscopic movies for study of organic molecules, assemblies, and reactions: The first 10 years of development. *Acc. Chem. Res.* **50**, 1281–1292 (2017).
34. H. Zheng, R. K. Smith, Y.-W. Jun, C. Kisielowski, U. Dahmen, A. P. Alivisatos, Observation of single colloidal platinum nanocrystal growth trajectories. *Science* **324**, 1309–1312 (2009).
35. H.-G. Liao, D. Zherebetskyy, H. Xin, C. Czarnik, P. Ercius, H. Elmlund, M. Pan, L.-W. Wang, H. Zheng, Facet development during platinum nanocube growth. *Science* **345**, 916–919 (2014).
36. N. D. Loh, S. Sen, M. Bosman, S. F. Tan, J. Zhong, C. A. Nijhuis, P. Král, P. Matsudaira, U. Mirsaidov, Multistep nucleation of nanocrystals in aqueous solution. *Nat. Chem.* **9**, 77–82 (2017).
37. F. M. Ross, Opportunities and challenges in liquid cell electron microscopy. *Science* **350**, aaa9886 (2015).
38. W. Gao, P. Tieu, C. Addiego, Y. Ma, J. Wu, X. Pan, Probing the dynamics of nanoparticle formation from a precursor at atomic resolution. *Sci. Adv.* **5**, eaau9590 (2019).
39. I. Lazić, E. G. T. Bosch, S. Lazar, Phase contrast STEM for thin samples: Integrated differential phase contrast. *Ultramicroscopy* **160**, 265–280 (2016).
40. I. Lazić, E. G. T. Bosch, "Analytical review of direct stem imaging techniques for thin samples" in *Advances in Imaging and Electron Physics*, P. W. Hawkes, Ed. (Elsevier, 2017), vol. 199, chap. 3, pp. 75–184.
41. S. de Graaf, B. J. Kooi, Radiation damage and defect dynamics in 2D WS_2: a low-voltage scanning transmission electron microscopy study. *2D Mater* **9**, 015009 (2022).
42. S. de Graaf, M. Ahmadi, I. Lazić, E. G. T. Boschb, J. Kooi, Imaging atomic motion of light elements in 2D materials with 30 kV electron microscopy. *Nanoscale* **13**, 20683–20691 (2021).
43. S. Ohba, S. Sato, Y. Saito, K.-I. Ohshima, J. Harada, Electron-density distribution in crystals of potassium tetrachloroplatinate(II) and influence of X-ray diffuse scattering. *Acta Cryst. B* **39**, 49–53 (1983).
44. H. Basch, H. B. Gray, Molecular orbital theory for square-planar metal halide complexes. *Inorg. Chem.* **6**, 365–369 (1967).
45. K. Persson, Materials Data on K2PtCl6 (SG:225) by Materials Project, Materials Project (2014); https://doi.org/10.17188/1199561.
46. X. Sang, A. A. Oni, J. M. Le Beau, Atom column indexing: Atomic resolution image analysis through a matrix representation. *Microsc. Microanal.* **20**, 1764–1771 (2014).
47. T. Krigas, M. T. Rogers, ESR study of radicals formed by irradiation of K2PtCl4 single crystals. *J. Chem. Phys.* **55**, 3035–3044 (1971).
48. G. E. Adams, R. B. Broszkiewicz, B. D. Michael, Pulse radiolysis studies on stable and transient complexes of platinum. *Trans. Faraday Soc.* **64**, 1256 (1968).
49. C. Wang, K. E. deKrafft, W. Lin, Pt Nanoparticles@Photoactive metal–organic frameworks: Efficient hydrogen evolution via synergistic photoexcitation and electron injection. *J. Am. Chem. Soc.* **134**, 7211–7214 (2012).
50. K. L. Y. Fung, S. T. Skowron, R. Hayter, S. E. Mason, B. L. Weare, N. A. Besley, Q. M. Ramasse, C. S. Allen, A. N. Khlobystov, Direct measurement of single-molecule dynamics and reaction kinetics in confinement using time-resolved transmission electron microscopy. *Phys. Chem. Chem. Phys.* **25**, 9092–9103 (2023).
51. J. Sloan, D. M. Wright, S. Bailey, G. Brown, A. P. E. York, K. S. Coleman, M. L. H. Green, J. Sloan, D. M. Wright, J. L. Hutchison, H.-G. Woo, Capillarity and silver nanowire formation observed in single walled carbon nanotubes. *Chem. Commun.*, 699–700 (1999).
52. R. F. Egerton, Control of radiation damage in the TEM. *Ultramicroscopy* **127**, 100–108 (2013).

53. L. Jones, S. Wenner, M. Nord, P. H. Ninive, O. M. Løvvik, R. Holmestad, P. D. Nellist, Optimising multi-frame ADF-STEM for high-precision atomic-resolution strain mapping. *Ultramicroscopy* **179**, 57–62 (2017).
54. J. Barthel, Dr. Probe: A software for high-resolution STEM image simulation. *Ultramicroscopy* **193**, 1–11 (2018).
55. G. Kresse, J. Furthmüller, Efficient iterative schemes for ab initio total-energy calculations using a plane-wave basis set. *Phys. Rev. B* **54**, 11169–11186 (1996).
56. G. Kresse, J. Furthmüller, Efficiency of ab-initio total energy calculations for metals and semiconductors using a plane-wave basis set. *Comput. Mater. Sci.* **6**, 15–50 (1996).
57. G. Kresse, D. Joubert, From ultrasoft pseudopotentials to the projector augmented-wave method. *Phys. Rev. B* **59**, 1758–1775 (1999).
58. J. P. Perdew, K. Burke, M. Ernzerhof, Generalized gradient approximation made simple. *Phys. Rev. Lett.* **77**, 3865–3868 (1996).
59. A. Jain, S. P. Ong, G. Hautier, W. Chen, W. D. Richards, S. Dacek, S. Cholia, D. Gunter, D. Skinner, G. Ceder, K. A. Persson, Commentary: The Materials Project: A materials genome approach to accelerating materials innovation. *APL Mater.* **1**, 011002 (2013).
60. W. Tang, E. Sanville, G. Henkelman, A grid-based Bader analysis algorithm without lattice bias. *J. Phys. Condens. Matter* **21**, 084204 (2009).

Acknowledgments

Funding: This work was supported by the National Science Foundation of China (23Z990201030). This work was performed, in part, at the Analytical Instrumentation Facility (AIF) at North Carolina State University, which is supported by the State of North Carolina and the National Science Foundation (award number ECCS-2025064). The AIF is a member of the North Carolina Research Triangle Nanotechnology Network (RTNN), a site in the National Nanotechnology Coordinated Infrastructure (NNCI). **Author contributions:** Conceptualization: W.G., J.G.S., Z.Z., K.J.S., J.P.G., and T.B.E. Methodology: J.G.S., W.G., K.J.S., Z.Z., and T.B.E. Investigation: J.G.S., K.J.S., W.G., Z.Z., and J.P.G. Visualization: J.G.S., K.J.S., and W.G. Supervision: W.G., J.P.G., Z.Z., and J.W. Writing—original draft: J.G.S. and W.G., and K.J.S. Writing—review and editing: W.G., J.G.S., Z.Z., and J.W. **Competing interests:** The authors declare they have no competing interests. **Data and materials availability:** All data needed to evaluate the conclusions in the paper are present in the paper and/or the Supplementary Materials.

Submitted 20 April 2023
Accepted 10 January 2024
Published 9 February 2024
10.1126/sciadv.adi0175